
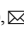


# Breaking the Fe<sub>3</sub>O<sub>4</sub>-wrapped copper microstructure to enhance copper–slag separation

Xiaopeng Chi<sup>1,2</sup>, Haoyu Liu<sup>1</sup>, Jun Xia<sup>1</sup>, Hang Chen<sup>3</sup>, Xiangtao Yu<sup>4</sup>, Wei Weng<sup>1,2</sup>,,  
and Shuiping Zhong<sup>1,2,3</sup>,

1) Zijin School of Geology and Mining, Fuzhou University, Fuzhou 350108, China

2) Fujian Key Laboratory of Green Extraction and High-Value Utilization of New Energy Metals, Fuzhou University, Fuzhou 350108, China

3) Zijin Mining Group Co., Ltd., Longyan 364200, China

4) Collaborative Innovation Center of Steel Technology, University of Science and Technology Beijing, Beijing 100083, China

(Received: 31 October 2023; revised: 16 February 2024; accepted: 22 February 2024)

**Abstract:** The precipitation of Fe<sub>3</sub>O<sub>4</sub> particles and the accompanied formation of Fe<sub>3</sub>O<sub>4</sub>-wrapped copper structure are the main obstacles to copper recovery from the molten slag during the pyrometallurgical smelting of copper concentrates. Herein, the commercial powdery pyrite or anthracite is replaced with pyrite–anthracite pellets as the reductants to remove a large amount of Fe<sub>3</sub>O<sub>4</sub> particles in the molten slag, resulting in a deep fracture in the Fe<sub>3</sub>O<sub>4</sub>-wrapped copper microstructure and the full exposure of the copper matte cores. When 1wt% composite pellet is used as the reductant, the copper matte droplets are enlarged greatly from 25 μm to a size observable by the naked eye, with the copper content being enriched remarkably from 1.2wt% to 4.5wt%. Density functional theory calculation results imply that the formation of the Fe<sub>3</sub>O<sub>4</sub>-wrapped copper structure is due to the preferential adhesion of Cu<sub>2</sub>S on the Fe<sub>3</sub>O<sub>4</sub> particles. X-ray photoelectron spectroscopy, Fourier transform infrared spectrometer (FTIR), and Raman spectroscopy results all reveal that the high-efficiency conversion of Fe<sub>3</sub>O<sub>4</sub> to FeO can decrease the volume fraction of the solid phase and promote the depolymerization of silicate network structure. As a consequence, the settling of copper matte droplets is enhanced due to the lowered slag viscosity, contributing to the high efficiency of copper–slag separation for copper recovery. The results provide new insights into the enhanced *in-situ* enrichment of copper from molten slag.

**Keywords:** pyrometallurgical smelting process; slag cleaning; reductants; copper matte

## 1. Introduction

As an indispensable element in many functional materials, copper possesses fascinating thermal and electronic conductivity [1–4]. Owing to the severe unbalance in the worldwide distribution of its resources, copper is viewed as a very important strategic metal by many nations. For example, China accounts for merely 5.53% of the copper resource on Earth [4–5]. Thus, the high efficiency and deep recovery of copper is of great importance.

The entrainment of copper matte droplets in molten slag commonly occurs during pyrometallurgical smelting and can be deteriorated by the excess precipitation of solid Fe<sub>3</sub>O<sub>4</sub> particles from the iron silicate-based molten slag [6–8]. This precipitation is inevitable due to the following reasons: (1) Fe<sub>3</sub>O<sub>4</sub> can easily be generated from the iron silicate molten slag because the smelting of copper concentrate is performed under an oxygen-enriched atmosphere [9–11]; (2) the melting point of Fe<sub>3</sub>O<sub>4</sub> is 1594°C, which is higher than the copper smelting temperature (1250–1300°C). The precipitated Fe<sub>3</sub>O<sub>4</sub> particles significantly increase the viscosity of the slag, pre-

venting slag-entrained copper matte (Cu<sub>2</sub>S–FeS) droplets from settling and resulting in increased copper loss in the slag due to restrained copper–slag separation [12–14]. In addition, the precipitated Fe<sub>3</sub>O<sub>4</sub> particles possess very strong hardness and tend to tightly wrap the copper matte droplets, hindering the coalescence between copper matte droplets in the molten slag [15–17] and blocking the high-efficiency recovery of copper during the subsequent grinding–flotation of cold slag [18–19].

Reducing the Fe<sub>3</sub>O<sub>4</sub> content of molten slag can promote copper–slag separation in the electric furnace for copper slag cleaning and hopefully enhance the subsequent recovery of copper from the cold slag during the following grinding–flotation [20–23]. Lowering the Fe<sub>3</sub>O<sub>4</sub> content is commonly realized by dropping carbon (coal or anthracite) [24] or pyrite (FeS<sub>2</sub>) as the reductant into the molten slag because the former possesses a strong reducing ability, and the latter is very cheap as the byproduct in the mineral process of copper ore [25–28]. However, carbon and pyrite are commonly separately used as reductants without considering the optimized tradeoff between cost and reducing ability [12,27,29]. In ad-

 Corresponding authors: Wei Weng E-mail: [wengwei198912@163.com](mailto:wengwei198912@163.com); Shuiping Zhong E-mail: [zpsu@163.com](mailto:zpsu@163.com)

© University of Science and Technology Beijing 2024

dition, both are used in their powdery state that generally floats on the surface of the molten slag and is easily blown away by the *in-situ* generated off-gas, especially carbon with low density, leading to very limited reaction kinetics [27,30]. The reductants in their powdery state tend to be flammable, increasing the operational risks. Enhancing the reaction kinetics of the reductants to eliminate the Fe<sub>3</sub>O<sub>4</sub> particles is an urgent but very challenging task.

Herein, a pelletized reductant was designed by mixing FeS<sub>2</sub> and anthracite powders and pressing the mixture into pellets to improve the reduction kinetics [31–34]. Such pelletized reductants with mixed components contribute to a good tradeoff between the cost and reducing ability and facilitate a deep reduction of Fe<sub>3</sub>O<sub>4</sub> particles in molten slag. Partially replacing anthracite with cheap pyrite can decrease the cost. The pelletized reductants are more difficult to blow away than their powdery counterparts, leading to a high utilization efficiency of the reductant. In this work, we conducted a detailed investigation into the effects of reductant dosage and reaction time and compared the use of different reducing agents as reductants in high-temperature settings. The microstructure of Fe<sub>3</sub>O<sub>4</sub>-wrapped copper was specifically studied, and the adsorption energy between iron oxides and copper matte was calculated using density functional theory (DFT). The lower Fe<sub>3</sub>O<sub>4</sub> content and large-size copper matte droplets, as well as fully exposed copper matte component, conjointly contribute to more efficient settling of copper matte for enrichment and hopefully benefit the copper recovery during the subsequent grinding–flotation

process of cold slag. The results can provide new insights into the enhancement of copper–slag separation in a molten state.

## 2. Experimental

### 2.1. Raw materials and chemical reagents

Copper slag was collected from a flash smelting furnace in the smelting plant in Zijin Mining Group Ltd. (Fujian Province, China). On-site sampling of the molten slag was conducted during the tapping of molten slag in the flash smelting furnace to restrain the overoxidation of the molten slag due to its contact with air. In addition, the molten slag was quenched in water to shorten its contact with air. The quenched slag was immediately transferred to an oven and vacuum dried to further inhibit its postoxidation. Table 1 lists the chemical composition of copper slag. Owing to its high magnetite content (12.4wt%), the copper content in the slag is 1.2wt%. Table 2 lists the chemical composition of anthracite and pyrite. The main component of pyrite is FeS<sub>2</sub>. Pyrite, anthracite, and Na<sub>2</sub>SiO<sub>3</sub> powders were weighed and mixed to prepare the composite reductant pellet. Na<sub>2</sub>SiO<sub>3</sub> (analytical grade, 99.7wt% in purity) was purchased from Sinopharm Chemical Reagent Co., Ltd. (China). Pyrite and anthracite were obtained from Guangzhou Dinghua Co., Ltd. (Guangzhou Province, China). The pyrite had a FeS<sub>2</sub> content of 91.06wt%, and the anthracite contained 73.8wt% fixed carbon, 11.7wt% volatile matter, 12.7wt% ash, and 1.4wt% moisture.

**Table 1. Chemical composition of copper slag**

									wt%
TFe	Cu	Fe <sub>3</sub> O <sub>4</sub>	SiO <sub>2</sub>	CaO	MgO	S	Al <sub>2</sub> O <sub>3</sub>	K <sub>2</sub> O	Cr <sub>2</sub> O <sub>3</sub>
39.1	1.2	12.4	34.3	2.5	1.3	0.9	2.40	0.80	0.23

**Table 2. Industrial analysis of the anthracite and pyrite**

					wt%
Material	Fixed carbon	Volatile matter	Ash	Moisture	Total sulfur
Anthracite	73.8	11.7	12.7	1.4	0.4
Material	FeS <sub>2</sub>	SiO <sub>2</sub>	2Fe(OH)SO <sub>4</sub>	KAl <sub>2</sub> [AlSi <sub>3</sub> O <sub>10</sub> ] [OH] <sub>2</sub>	Other
Pyrite	91.06	4.06	1.98	1.66	1.24

### 2.2. High-temperature tests

The reductant pellets were prepared as follows. First, the commercial pyrite and anthracite powders were thoroughly mixed and added with an extra 1wt% Na<sub>2</sub>SiO<sub>3</sub> as the binder. The mixture was pressed into pellets by die-pressing at 20 MPa. The size of the pressed pellets is 20 mm in diameter. For simplification, the term “pyrite + anthracite pellet” was abbreviated as “(FeS<sub>2</sub>+C) pellet.” In our previous experiments, a mass ratio of 2.33 was observed between FeS<sub>2</sub> and anthracite, a balance between the chemical reducing ability and the density-induced physical settling of the pellets. Without specific notes, the mass ratio of pyrite/anthracite in the pellet was fixed at 2.33.

High-temperature experiments were performed in a vertical tube furnace. The slag was milled in a ball mill to obtain

a mean particle size of 75 μm. Approximately 300 g of dry copper slag was homogeneously mixed and transferred into a corundum crucible (φ60 mm × 100 mm). The crucible was then transferred to the constant temperature area of the furnace and heated to 1250°C at 10°C·min<sup>-1</sup> under an Ar flow (1 L·min<sup>-1</sup>). After being heated for 30 min to fully melt the slag, the reductant pellets were dropped into the crucible from the top of the furnace. After the experiment, the temperature was cooled to 900°C at 5°C·min<sup>-1</sup>, followed by natural cooling to room temperature. The heating and cooling rates were kept the same for all samples to enable the same crystallization behavior. In this way, the prior decomposition of FeS<sub>2</sub> can be avoided during the heating. After the experiment, the aluminum content was increased from 1.25wt% to 1.38wt% due to the corrosion of the corundum crucible [12,35]. Commercial pyrite and anthracite in a

powdery state were also separately used as the reductants for comparison and delivered through a corundum tube ( $d = 15$  mm). A slag sample kept at  $1250^{\circ}\text{C}$  without adding any reductants was also prepared for comparison. For simplification, the reductant-free experiment was denoted as test 1. Correspondingly, test 2, test 3, and test 4 pointed to the cases using commercial pyrite powder, anthracite powder, and composite pellets as the reductants, respectively. The amounts of added reductants for test 2, test 3, and test 4 were all fixed at 1wt%.

### 2.3. Characterizations

The copper content in all the samples was determined using an atomic absorption spectrometer (AA-6880, Shimadzu, Japan). The magnetite content was measured by magnetic

susceptibility technique using a SATMAGAN 135 instrument with an accuracy of 0.4% over the measurement range. The phase composition of the slag sample was detected using an X-ray diffractometer (XRD, D8 Advance, Bruker, German). The microstructures and distribution of each slag sample were determined using a scanning electron microscope (SEM, Pure, USA) and an energy dispersive spectroscope (EDS, Pure, USA). X-ray photoelectron spectroscopy (XPS) analysis was performed with a Thermo ESCALAB 250XI instrument using an Al  $K_{\alpha}$  X-ray source. All the XPS spectra were calibrated to the C 1s peak of adventitious carbon positioned at 284.8 eV. A nonlinear least-squares curve-fitting program (Advantage software 5.52) was used to deconvolute the XPS data. The detailed fitting parameters for the XPS spectra of all the samples are presented in Table 3.

**Table 3. Fitting parameters for the XPS spectra of Fe 2p<sup>3/2</sup>**

Phase	Baseline approximation	Synthetic peak shape approximation	Peak position / eV	Full width at half maximum (FWHM) for different samples
FeO	Shirley	Gaussian (80%)–Lorentzian (20%)	710.30	C powder: 2.86 FeS <sub>2</sub> powder: 2.61 (FeS <sub>2</sub> +C) pellet: 3.00
Fe <sub>3</sub> O <sub>4</sub>	Shirley	Gaussian (80%)–Lorentzian (20%)	711.40	C powder: 2.84 FeS <sub>2</sub> powder: 3.50 (FeS <sub>2</sub> +C) pellet: 3.50
Fe <sub>2</sub> SiO <sub>4</sub>	Shirley	Gaussian (80%)–Lorentzian (20%)	713.43	C powder: 3.40 FeS <sub>2</sub> powder: 2.31 (FeS <sub>2</sub> +C) pellet: 3.50

Eighteen low-magnification SEM images were taken for statistical analysis to gain insight into the thickness variation of the Fe<sub>3</sub>O<sub>4</sub> shell on the Fe<sub>3</sub>O<sub>4</sub>-wrapped copper particles after slag cleaning. The diameter of Fe<sub>3</sub>O<sub>4</sub>-wrapped copper particles and the thickness of the Fe<sub>3</sub>O<sub>4</sub> shell were calculated by Nano Measurer 1.2 software. The extent ( $\alpha$ ) of each copper matte encapsulation by Fe<sub>3</sub>O<sub>4</sub> and the corresponding average value ( $\gamma$ ) were statistically evaluated using Eqs. (1) and (2):

$$\alpha = \frac{l}{L} \quad (1)$$

$$\gamma = \sum_{i=1}^n \frac{\alpha_i}{n} \quad (2)$$

where  $l$  is the thickness of the Fe<sub>3</sub>O<sub>4</sub> shell,  $L$  is the diameter of Fe<sub>3</sub>O<sub>4</sub>-wrapped copper particles, and  $n$  is the number of Fe<sub>3</sub>O<sub>4</sub>-wrapped copper particles for statistical analysis. Each Fe<sub>3</sub>O<sub>4</sub>-wrapped copper particle was measured three times for accuracy.

The liquid viscosity  $\mu$  of different solid-phase contents was calculated using Eq. (3), which describes the viscous behavior of liquid melts containing solid phases [29,36]. The phase diagram was calculated using Factsage 8.1 (GTT-Technologies, Germany) against the databases FactPS, FToxid, and FTmisc. The metal oxides in copper slag can greatly affect the phase. Therefore, the concentrations of main metal oxides (Al<sub>2</sub>O<sub>3</sub>, CaO, K<sub>2</sub>O, MgO, and Cr<sub>2</sub>O<sub>3</sub>) in the original slag were fixed based on the values in Table 1 for calculation.

$$\mu = \mu_s \left( 1 + \frac{5}{2} f \right) \quad (3)$$

where  $\mu_s$  is the viscosity of particle-free slag at  $1250^{\circ}\text{C}$ , Pa·s, and  $f$  is the volume fraction of solid phase in the molten slag, %.

The reduction efficiency of Fe<sub>3</sub>O<sub>4</sub> was calculated as follows:

$$\varepsilon = \frac{m_o - m_r}{m_o} \times 100\% \quad (4)$$

where  $\varepsilon$  is the reduction efficiency of Fe<sub>3</sub>O<sub>4</sub>, %;  $m_o$  is the mass of Fe<sub>3</sub>O<sub>4</sub> in the original slag before reduction, g;  $m_r$  is the mass of Fe<sub>3</sub>O<sub>4</sub> in the slag sample after reduction, g.

The structure of slag samples was analyzed by Fourier transform infrared spectrometer (FTIR) (IS10, Nicolet, America) and Raman spectroscope (inVia, Renishaw, Britain). The excitation laser source with a wavelength of 632.8 nm was used for Raman analysis, and the spectrum ranging from 400 to 2000  $\text{cm}^{-1}$  was collected. The range within 800–1150  $\text{cm}^{-1}$  was determined to be a symmetric stretching vibration band of the silicon–oxygen tetrahedron [37]. Q<sup>0</sup> (SiO<sub>4</sub><sup>4-</sup>), Q<sup>1</sup> (Si<sub>2</sub>O<sub>7</sub><sup>6-</sup>), Q<sup>2</sup> (Si<sub>2</sub>O<sub>6</sub><sup>4-</sup>), and Q<sup>3</sup> (Si<sub>2</sub>O<sub>5</sub><sup>2-</sup>) represent monomer, dimer, chain, and sheet, respectively [37–39]. The wavenumbers in the regions of 850–870, 900–920, 950–1000, and 1000–1100  $\text{cm}^{-1}$  represent the characteristic frequencies of Q<sup>0</sup>, Q<sup>1</sup>, Q<sup>2</sup>, and Q<sup>3</sup>, respectively, which can be used for analyzing the silicate network structure of slags. The detailed fitting parameters for the Raman spectra of all samples are presented in Table 4.

**Table 4.** Fitting parameters for the Raman spectra

[SiO <sub>4</sub> ] <sup>4-</sup> tetrahedral band	Baseline approximation	Synthetic peak shape approximation	Peak position / cm <sup>-1</sup>	FWHM for different samples
Q <sup>0</sup>	Line	Gaussian	843.4	C powder: 54.5 FeS <sub>2</sub> powder: 51.4 (FeS <sub>2</sub> +C) pellet: 56.7
Q <sup>1</sup>	Line	Gaussian	908.2	C powder: 26.9 FeS <sub>2</sub> powder: 52.6 (FeS <sub>2</sub> +C) pellet: 39.7
Q <sup>2</sup>	Line	Gaussian	953.5	C powder: 44.7 FeS <sub>2</sub> powder: 26.2 (FeS <sub>2</sub> +C) pellet: 87.5
Q <sup>3</sup>	Line	Gaussian	1011.7	C powder: 94.5 FeS <sub>2</sub> powder: 80.7 (FeS <sub>2</sub> +C) pellet: 90

## 2.4. DFT calculations

The vienna *ab initio* simulation package with the project-augmented wave method and the Perdew–Burke–Ernzerhof functional for the exchange–correlation term was adopted for the DFT calculations. The value of 400 eV was chosen for the kinetic energy cut-off of the electron wave functions. The convergence tolerances of the energy and forces were set to be  $1 \times 10^{-4}$  eV and  $0.5 \text{ eV} \cdot \text{nm}^{-1}$ , respectively [40–42]. The van der Waals interactions were considered by the DFT-D3 dispersion correction method. In particular, the (311) crystal plane for solid Fe<sub>3</sub>O<sub>4</sub>, (200) crystal plane for precipitated FeO, and the (112) crystal plane for precipitated Fe<sub>2</sub>SiO<sub>4</sub> at the cooling state were adopted for calculating the adsorption behaviors of the Cu<sub>2</sub>S molecules because the above crystal planes point to the strongest peaks in the XRD patterns of the corresponding oxides [43–44].

The free energy was calculated using the following equation [45]:

$$G = E + E_{zp} - TS \quad (5)$$

where  $G$ ,  $E$ ,  $E_{zp}$ ,  $T$ , and  $S$  are the free energy, total energy

from DFT calculations, zero-point energy, temperature ( $T$  was set to be 1523.15 K), and entropic respectively.

$E_{zp}$  and  $TS$  were respectively calculated by the following equations [46–47]:

$$E_{zp} = \frac{1}{2} \sum_i h\nu_i \quad (6)$$

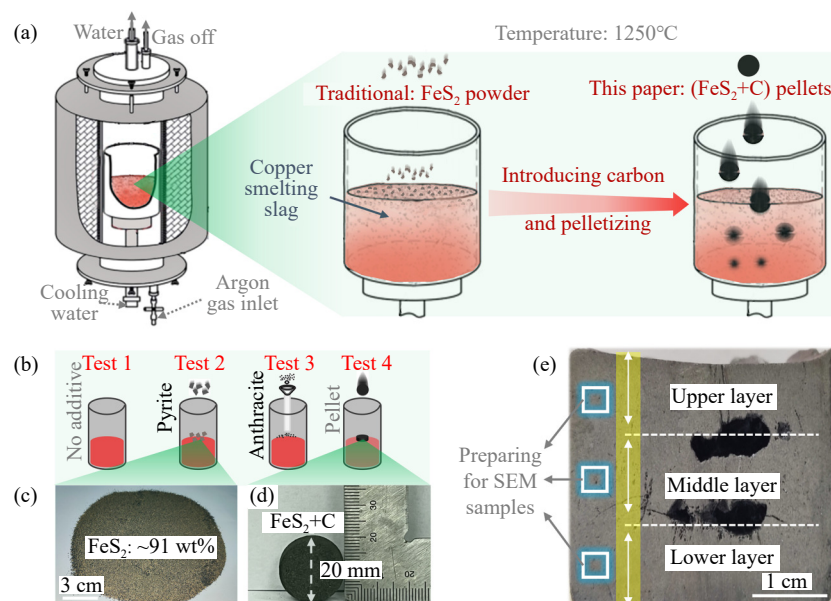
$$TS = k_B T \left[ \sum_i \ln \left( \frac{1}{1 - e^{-h\nu_i/(k_B T)}} \right) + \sum_i \frac{h\nu_i}{k_B T} \frac{1}{(e^{h\nu_i/(k_B T)} - 1)} + 1 \right] \quad (7)$$

where  $h$  is the Planck constant ( $6.62607015 \times 10^{-34} \text{ J} \cdot \text{s}$ ),  $\nu$  is the vibrational frequency, and  $k_B$  is the Boltzmann constant ( $1.380649 \times 10^{-23} \text{ J} \cdot \text{K}^{-1}$ ).

## 3. Results and discussion

### 3.1. Properties of the slag and reductants

The detailed procedure for the experiments is illustrated in Fig. 1. For some copper smelters in industry, the FeS<sub>2</sub> powders directly added to the molten slags tend to float on the upper surface of the melt. Herein, replacing pyrite powder



**Fig. 1.** (a) Illustration for the high-temperature experimental setup and reductants; (b) illustrations for the settling of copper matte liquid in molten slags in four different cases; (c, d) optical images for FeS<sub>2</sub> powder and (FeS<sub>2</sub>+C) pellet; (e) typical optical images after experiment and the corresponding sampling rule.



with (FeS<sub>2</sub>+C) pellets can hopefully facilitate the reductants to sink smoothly into the molten slag (Fig. 1(a)). The pelletized reductant with elaborately adjusted density can be added into the flash furnace from the top of the settler, which usually possesses several opening holes for adding iron bars or measuring the slag viscosity. The four experiments, namely, reductant-free (test 1), pyrite powder (test 2), anthracite powder (test 3), and (FeS<sub>2</sub>+C) pellet (test 4), are illustrated in Fig. 1(b), with the optical photos of pyrite powder and (FeS<sub>2</sub>+C) pellet shown in Fig. 1(c) and (d), respectively. After the experiments, the solidified slags were sliced into three layers (Fig. 1(e)) and then separately crushed into powders for analysis, in which the copper contents in the lower and upper layers were first determined.

The mixed components for the reductant and Fe<sub>3</sub>O<sub>4</sub>-wrapped copper microstructure in the slag were verified by characterizing the pellet reductant and the original copper slag. XRD results for the mixed components of the pellet reductant revealed the well indexed peaks for FeS<sub>2</sub> (PDF#71-

2219) and the bulk peak at 26° for carbon (Fig. 2(a)). The slag (Fig. 2(b)) mainly consisted of fayalite (Fe<sub>2</sub>Si<sub>2</sub>O<sub>4</sub>) and magnetite (Fe<sub>3</sub>O<sub>4</sub>). No peaks for Cu<sub>2</sub>S were detected in the XRD patterns (Fig. 2(b)) because the trace amounts of copper matte were tightly wrapped by the precipitated Fe<sub>3</sub>O<sub>4</sub> particles (Fig. 2(c) and (d)). Such Fe<sub>3</sub>O<sub>4</sub>-wrapped copper microstructure was further manifested by the EDS results (Fig. 2(e)), with the core in point 1 (Fig. 2(d)) being Cu<sub>2</sub>S and the shell in point 2 (Fig. 2(d)) being Fe<sub>3</sub>O<sub>4</sub>. The contents of point 1 and 2 are shown in Table 5. The closely wrapped copper matte was also emphasized by the concentrated distribution of Cu on the core (Fig. 2(f)), surrounded by Fe and O (Fig. 2(g) and (h)) and free of Si on the shell (Fig. 2(i)). The characterizations confirm that the (FeS<sub>2</sub>+C) mixed pellets as the reductant were successfully prepared, and the copper matte droplets in the copper slag were closely wrapped by the precipitated Fe<sub>3</sub>O<sub>4</sub> particles. Such Fe<sub>3</sub>O<sub>4</sub>-wrapped copper microstructure can possibly hinder the settling of copper droplets during pyrometallurgical smelting.

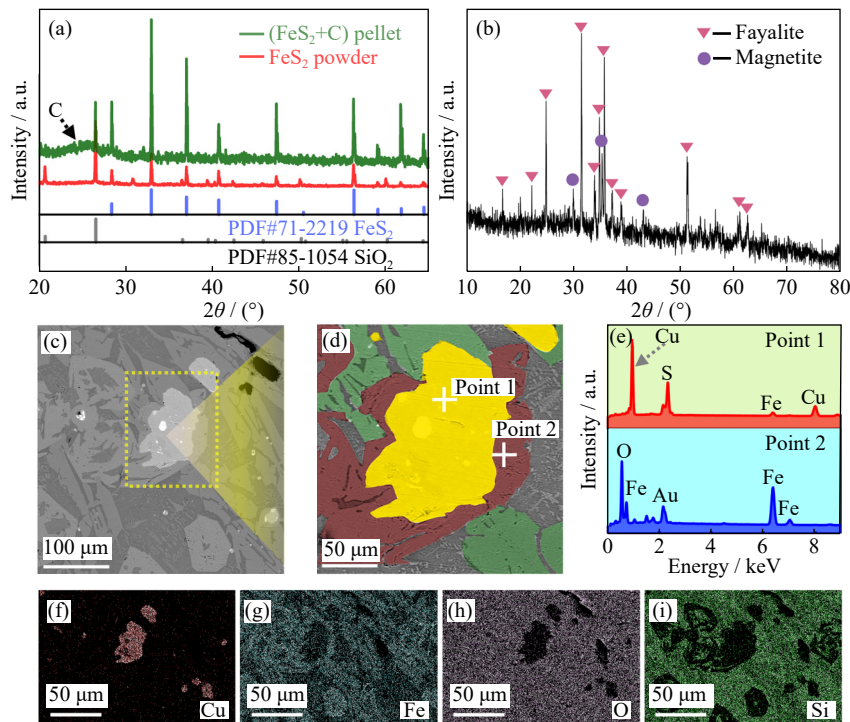


Fig. 2. Characterizations for the reductants and raw copper slag: (a) XRD patterns of the pyrite powder and (FeS<sub>2</sub>+C) pellet; (b) XRD pattern of the original copper slag; (c) SEM of the original copper slag; (d) magnification of the square area in (c); (e) EDS results of point 1 and point 2 in (d); (f–i) element mappings of Cu, Fe, O, and Si.

Table 5. Energy spectrum analysis of Fig. 2(d) wt%

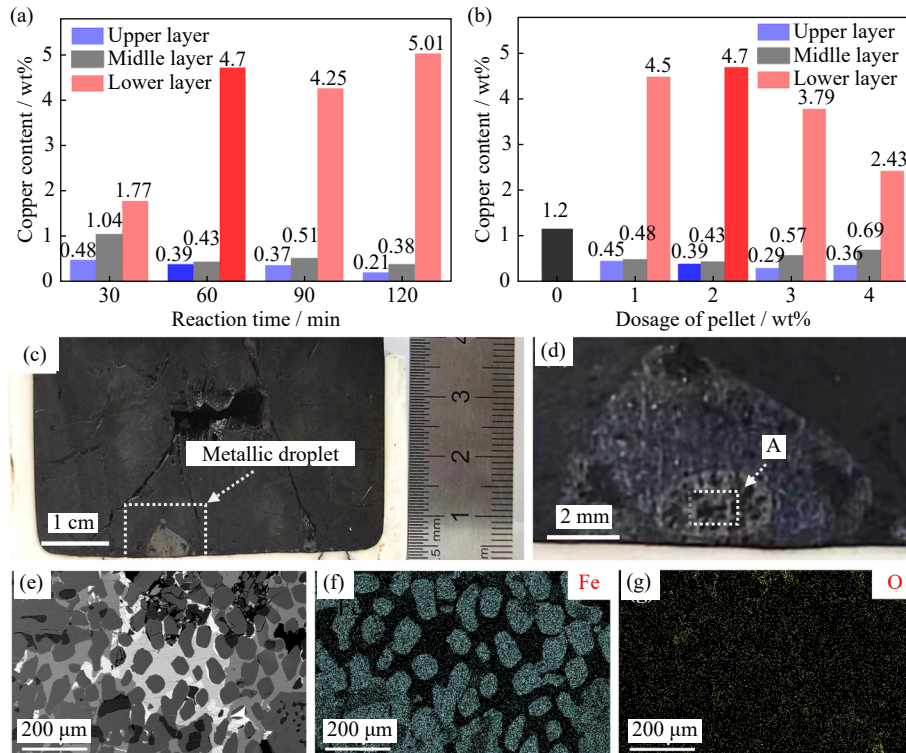
Point	Cu	S	Fe	O	Au	Si
1	67.9	27.8	4.3	—	—	—
2	—	—	71.5	26.7	1.1	0.7

### 3.2. Breaking the Fe<sub>3</sub>O<sub>4</sub>-wrapped copper structure by promoting Fe<sub>3</sub>O<sub>4</sub> reduction

Fig. 3(a) shows the slag cleaning results of various reaction times and (FeS<sub>2</sub>+C) pellet dosages. When the reaction time was increased from 30 to 120 min, the copper content in

the upper and middle slag layers decreased from 0.48wt% to 0.21wt% and from 1.04wt% to 0.38wt%, respectively (Fig. 3(a)). Meanwhile, the copper content in the lower slag layer increased from 1.77wt% to 5.01wt% (Fig. 3(a)). There is only a slight improvement in the settling of copper matte droplets when comparing the 60 and 120 min reaction times. For the balance between slag cleaning efficiency and the associated energy consumption, the desirable reaction time was fixed at 60 min.

Fig. 3(b) shows the effect of (FeS<sub>2</sub>+C) pellet dosage on the copper content in the slag. By increasing the (FeS<sub>2</sub>+C) pellet



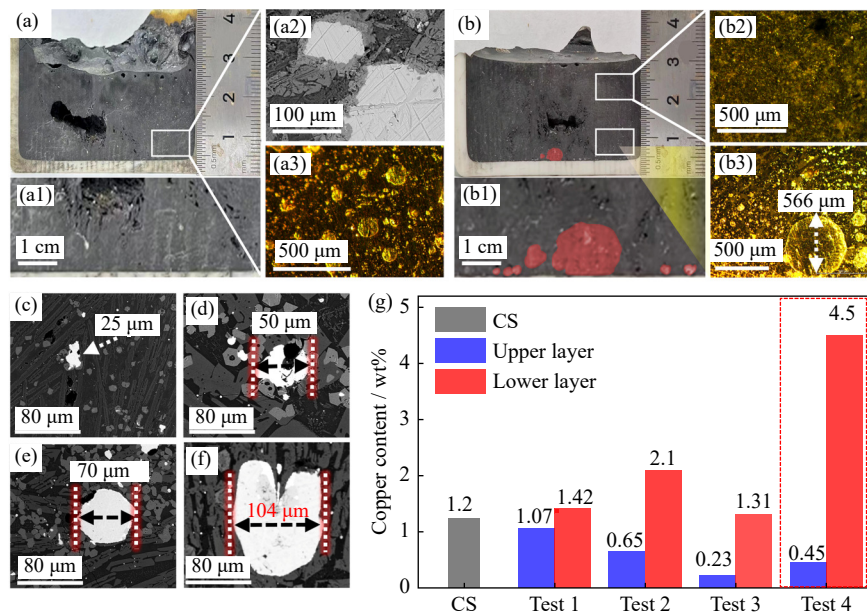
**Fig. 3.** (a, b) Effects of high-temperature test parameters on the slag cleaning results: (a) reaction time (reaction temperature of 1250°C, pellet dosage of 2wt%) and (b) dosage of (FeS<sub>2</sub>+C) pellets (reaction temperature of 1250°C, reaction time of 60 min); (c) optical images of the slag sample after reaction with 4wt% (FeS<sub>2</sub>+C) pellets; (d) magnified view of the metallic droplet in (c); SEM image (e) and elemental distribution mappings (f, g) of the area “A” in (d).

dosage, the copper content in the upper and middle slag layers decreased significantly at first. However, when the (FeS<sub>2</sub>+C) pellet dosage exceeded 2wt%, the enrichment of copper matte in the lower slag layer decreased gradually. Meanwhile, increasing the pellet dosage from 1wt% to 2wt% did not significantly enhance the settling of copper matte. Further increasing the dosage to 4wt% led to the generation of metallic particles at the bottom of the slag (Fig. 3(c) and (d)), which mainly consisted of metallic iron (Fig. 3(e)–(g)). Adding excess amounts of pellets resulted in the reduction of a part of FeO to metallic Fe, leading to a decrease in the FeO/SiO<sub>2</sub> ratio in the slag and suppressing the settling of matte droplets due to the increased slag viscosity. After the added dosage was fixed at 1wt%, the pellets with various mass ratios of pyrite/anthracite were also tested. The results reveal that 2.33 pellet composition was the optimized value, producing the most desirable reaction kinetics.

The promoted size growth of copper matte droplets after replacing the powdery pyrite with the (FeS<sub>2</sub>+C) pellets was further disclosed by optical observations. Fig. 4(a) shows that after reduction by the pyrite powder, no clear copper matte droplets were found on the bottom of the cross-section image (Fig. 4(a) and (a1)). After crushing the slag sample, no copper particles were found by the naked eye. The magnification of the bottom area presents copper matte droplets being wrapped by Fe<sub>3</sub>O<sub>4</sub> (Fig. 4(a2)), indicating insufficient Fe<sub>3</sub>O<sub>4</sub> reduction by the pyrite powder. The largest size of copper matte droplets in the bottom regions of the slag was approximately 125 μm (Fig. 4(a3)). After the pyrite powder was re-

placed with the (FeS<sub>2</sub>+C) pellets, a sharp increase was observed in the copper matte size in the bottom region of the slag, with copper matte droplets as large as 0.5 mm easily visualized by the naked eye (Fig. 4(b) and (b1)). Owing to its enrichment, the copper matte (Fig. 4(b1)) was easily separated from tailings by crushing the slag sample. The microscope image shows that very limited copper matte droplets can be detected in the upper regions of the slag (Fig. 4(b2)). Instead, copper matte droplets larger than 500 μm can be easily found at the bottom regions with the naked eye (Fig. 4(b3)). The promoted size growth of the copper matte was also revealed by the SEM images (Fig. 4(c)–(f)), with the size for the typical copper matte droplet increasing from 25 μm for original copper slag (CS) (Fig. 4(c)) to 50 μm for the pure anthracite (Fig. 4(d)), 70 μm for the Fe<sub>2</sub>S-treated case (Fig. 4(e)), and 104 μm for the (FeS<sub>2</sub>+C) pellet-treated case (Fig. 4(f)). The above results are further underlined by the copper contents in different layers of the solidified slag after reaction (Fig. 4(g)), showing that the copper content in the lower layer of test 4 (FeS<sub>2</sub>+C pellets) ranked the highest (4.5wt%) and greatly exceeded all other tests. Correspondingly, the copper content in the upper layer for test 4 was the lowest (0.45wt%), again proving the enhanced copper–slag separation in the case of the (FeS<sub>2</sub>+C) pellets.

The (FeS<sub>2</sub>+C) pellets as the composite reductant showed a more efficient reduction of Fe<sub>3</sub>O<sub>4</sub> particles than the pyrite powders and anthracite used in copper slag cleaning. As shown in Fig. 5(a), pyrite spontaneously decomposed to FeS, reducing the unfavored Fe<sub>3</sub>O<sub>4</sub> particles to favorable Fe<sub>2</sub>SiO<sub>4</sub>



**Fig. 4.** (a, a1) Optical images of the slags after reaction with pyrite powder: (a) entire cross-sectional image and (a1) bottom-edge image. (a2) SEM image and (a3) optical microscope image in the bottom-edge region of (a). (b, b1) Optical images of the slags after reaction with (FeS<sub>2</sub>+C) pellets: (b) entire cross-sectional image and (b1) bottom-edge image. (b2, b3) Optical microscope images for (b2) top-edge region and (b3) bottom-edge region. (c–f) Copper matte size in lower layer: (c) reductant-free, (d) reduced by anthracite, (e) reduced by pyrite powder, and (f) reduced by (FeS<sub>2</sub>+C) pellets. (g) Copper content of various samples (CS: original copper slag; test 1: without reductant but undergoing the same melting–solidification; test 2: using the pyrite powder as the reductant; test 3: using the anthracite powder as the reductant; test 4: using the (FeS<sub>2</sub>+C) pellet as the reductant).

at temperatures higher than 1167°C [48–49]. Meanwhile, carbon facilitated the conversion of Fe<sub>3</sub>O<sub>4</sub> particles at a low temperature of 686°C (Fig. 5(a)), indicating that Fe<sub>3</sub>O<sub>4</sub> is more easily reduced by the (FeS<sub>2</sub>+C) composite than the single pyrite component from a thermodynamic perspective [48–49]. The above results were also manifested by the settling tests using various reductants. In the single pyrite case (test 2 in Fig. 5(b)), the reduction efficiency of Fe<sub>3</sub>O<sub>4</sub> was 37.6% for the upper layer and 22.5% for the lower layer. The reduction efficiency of Fe<sub>3</sub>O<sub>4</sub> is higher in the upper layer than in the lower layer, implying that the powdery pyrite mainly floats on the upper part of the molten slag despite the higher density of the former than the latter (FeS<sub>2</sub> density: 5.0 g·cm<sup>-3</sup>; slag density: 3.4 g·cm<sup>-3</sup>) [50]. Such a phenomenon was highly evident for the low-density anthracite case (test 3 in Fig. 5(b)), revealing the lowest reduction efficiency of 9.8% in the lower layer and the highest reduction efficiency of Fe<sub>3</sub>O<sub>4</sub> in the upper layer in all cases. This finding again highlights that anthracite possesses the strongest reducing ability but the most unfavorable reaction kinetics due to difficulties in sinking into the molten slag (slag density: 3.4 g·cm<sup>-3</sup>; anthracite density: 1.4 g·cm<sup>-3</sup>) [51]. Compared with the pyrite powder (test 2) and anthracite (test 3), the (FeS<sub>2</sub>+C) pellet (test 4 in Fig. 5) produced different results, namely, a higher reduction efficiency of Fe<sub>3</sub>O<sub>4</sub> in the lower layer than in the upper layer. This result indicates that the (FeS<sub>2</sub>+C) pellet can smoothly sink into the molten slag rather than float on the upper layer, providing favorable reaction kinetics. In addition, the reduction efficiency of Fe<sub>3</sub>O<sub>4</sub> in the lower layer for test 4 was the highest, also stressing the superior reaction kinetics in test 4.

The more favorable ability of the (FeS<sub>2</sub>+C) pellet for eliminating Fe<sub>3</sub>O<sub>4</sub> than pyrite powder and anthracite was also proven by the XRD results of the posttreated slags. As shown in Fig. 5(c)–(f), the trend for the diffraction intensity of Fe<sub>3</sub>O<sub>4</sub> in the upper layer was consistent with the Fe<sub>3</sub>O<sub>4</sub> contents in Fig. 5(b). In particular, the lower part for test 4 (Fig. 5(g)–(j)) showed the weakest diffraction intensity of Fe<sub>3</sub>O<sub>4</sub>, again implying that the (FeS<sub>2</sub>+C) pellets have the most fascinating reaction kinetics for eliminating Fe<sub>3</sub>O<sub>4</sub> among the tested reductants.

A comparison of the changes in copper contents and microstructure is provided in Fig. 6. Bright copper matte droplets were found in the upper layers when using pyrite (Fig. 6(a)) or anthracite powder as the reductant (Fig. 6(b)). However, when the (FeS<sub>2</sub>+C) pellets were used (Fig. 6(c)), the bright copper matte droplets were hardly observed, indicating they have smoothly settled in this case. The middle layers exhibited the same results as the upper layers (Fig. 6(d)–(f)), also manifesting the enhanced sedimentation of copper matte droplets when using the (FeS<sub>2</sub>+C) pellets as the reductant. In the lower layer, bright copper matte droplets in large sizes were observed for the (FeS<sub>2</sub>+C) pellets (Fig. 6(g)–(i)), again validating the smoother settling and agglomeration of copper matte droplets when using the (FeS<sub>2</sub>+C) pellet than the other two reductants. Correspondingly, the copper content was the highest in the lower layer and the lowest in the upper layer for the (FeS<sub>2</sub>+C) pellet case among the three tested cases (Fig. 4(g)).

As shown in Fig. 7(a)–(c), the cross-sectional (Fig. 7(a)) and top-view (Fig. 7(b)) images of the quenched slag samples reveal that the pure anthracite pellet tended to float on the up-



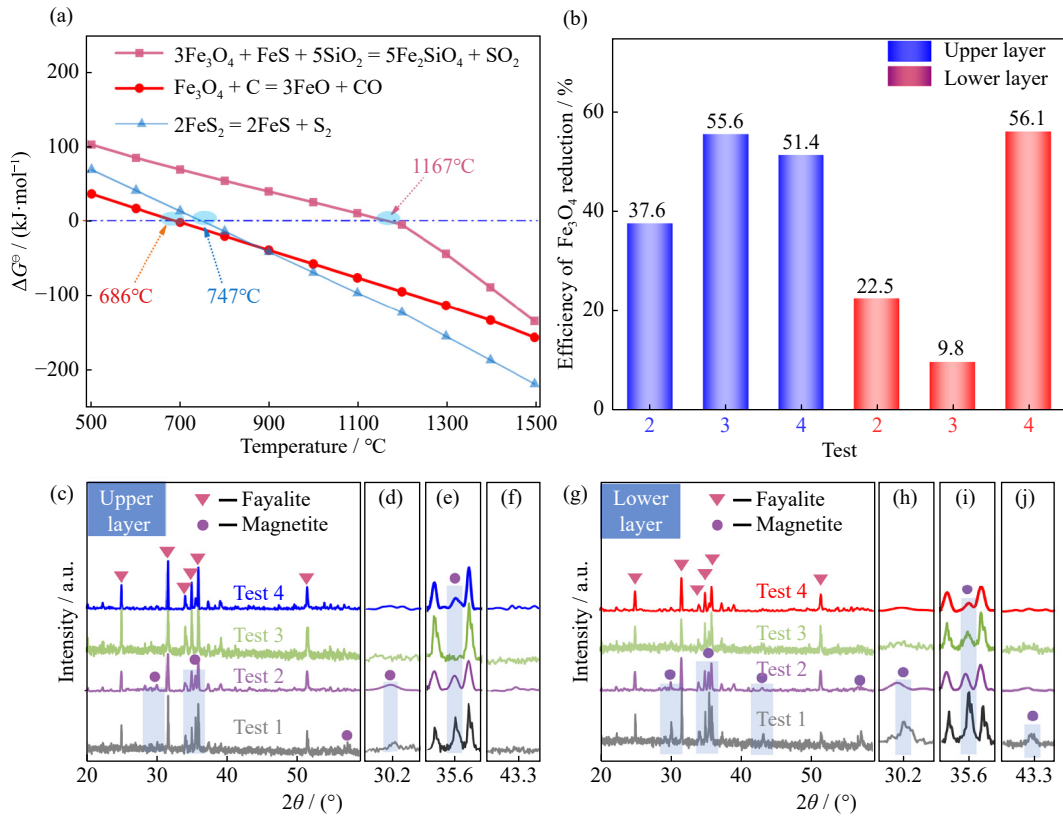


Fig. 5. (a) Standard Gibbs free energies of related reactions (all the activities of related chemicals were set to 1 for calculations); (b) efficiency of Fe<sub>3</sub>O<sub>4</sub> reduction in test 2 (FeS<sub>2</sub> powder as reductant), test 3 (anthracite powder as reductant), and test 4 ((FeS<sub>2</sub>+C) pellet as reductant); (c–f) XRD patterns of the slags in the upper layer after reactions; (g–j) XRD patterns of the slags in the lower layer after reactions.

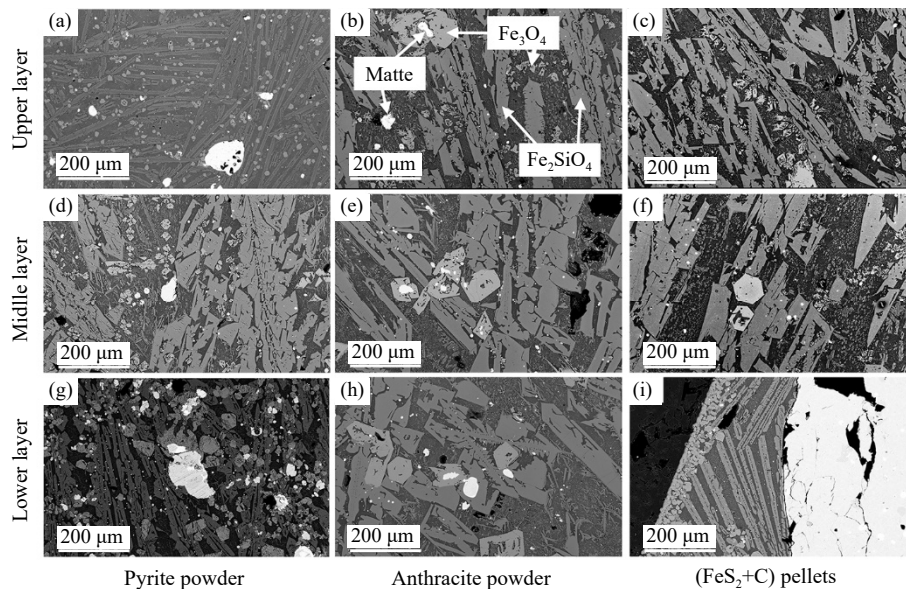
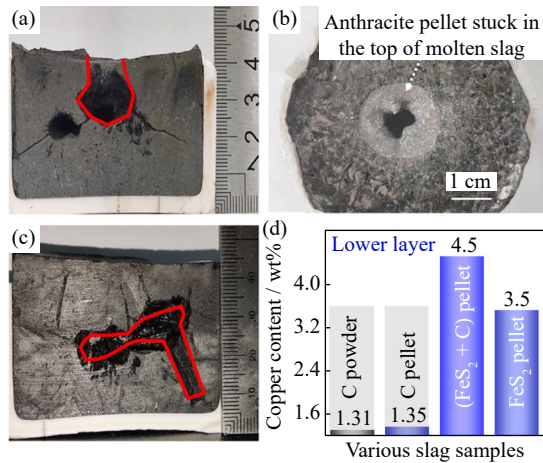


Fig. 6. SEM images of the slags after reaction with various reductants: (a, d, and g) using pyrite as reductant: (a) upper layer, (d) middle layer, and (g) lower layer; (b, e, and h) using anthracite powder as reductant: (b) upper layer, (e) middle layer, and (h) lower layer; (c, f, and i) using (FeS<sub>2</sub>+C) pellets as reductant: (c) upper layer, (f) middle layer, and (i) lower layer.

per surface of molten slag. Meanwhile, Fig. 7(c) illustrates that the (FeS<sub>2</sub>+C) composite pellet (density: 3.8 g·cm<sup>-3</sup>) can smoothly drop into the interior sites, manifesting the density-dependent floating and sinking phenomena. The (FeS<sub>2</sub>+C) composite pellets presented a strong ability to promote the settling of copper matte droplets in the molten slag.

Moreover, the settling behavior of copper matte was slightly enhanced by converting the powdery pyrite or anthracite into pelletized ones. As shown in Figs. 7(d) and 4(g), the enrichment of copper at the lower slag layer again proved that the pelletizing and (FeS<sub>2</sub>+C) mixing strategies can facilitate the separation between copper matte droplets and slag.





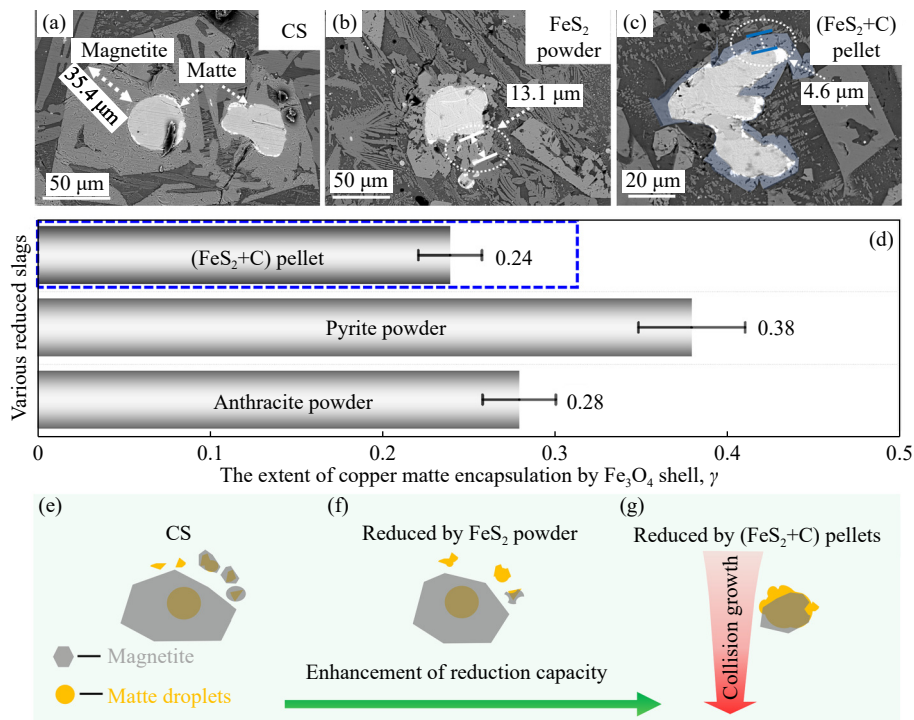
**Fig. 7.** (a–c) Optical images of quenched slag samples: (a) cross-sectional image of anthracite pellet as the reductant; (b) top view of (a); (c) cross-sectional image of the (FeS<sub>2</sub>+C) pellet as the reductant; (d) effect of various kinds of reductant pellets and anthracite powder as the reductant on Cu content in the lower slag layer.

The abundance of large dendrites away from the copper matter droplets in the SEM images implies that some Fe<sub>3</sub>O<sub>4</sub> molecules that exist in a soluble state in molten slag are precipitated during the cooling [17]. Compared with that reduced by the pyrite or anthracite powder, the smoother reduction of Fe<sub>3</sub>O<sub>4</sub> by the as-prepared (FeS<sub>2</sub>+C) pellets contributes to the full exposure of the Fe<sub>3</sub>O<sub>4</sub>-wrapped copper matte droplets. As shown in Fig. 8(a), the thickness of the Fe<sub>3</sub>O<sub>4</sub> shell for wrapping one typical copper matte droplet was as high as 35.4 μm in the original copper slag, which decreased

to 13.1 μm when using the powdery pyrite as the reductant (Fig. 8(b)). When the (FeS<sub>2</sub>+C) pellets were used as the reductants (Fig. 8(c)), the thickness of the Fe<sub>3</sub>O<sub>4</sub> shell further decreased to lower than 4.6 μm, with many edges of the copper matte droplet in the core being exposed. Therefore, mixing carbon with pyrite can provide a strong reducing ability, and die-pressing the powders into pellets enables good reaction kinetics. The SEM images show no difference between the pure anthracite-treated slag in the lower layer and the original slag because the Fe<sub>3</sub>O<sub>4</sub> content in the lower layer (Fig. 5 (b)) shows negligible changes compared with that of the original slag (Table 1) Therefore, the SEM images for the pure anthracite case are not presented in Fig. 8.

The statistical analysis in Fig. 8(d) shows the same results as Fig. 8(a)–(c). The typical Fe<sub>3</sub>O<sub>4</sub> encapsulation structures are detailed for different samples in Fig. 8(a)–(c). As shown in Fig. 8(d), the Fe<sub>3</sub>O<sub>4</sub> encapsulation extent for the copper matte droplets was 0.24 for the (FeS<sub>2</sub>+C) pellet, 0.28 for the anthracite powder, and 0.38 for the pyrite powder, proving the stronger ability of the (FeS<sub>2</sub>+C) pellet for breaking the Fe<sub>3</sub>O<sub>4</sub>-wrapped copper matte structure. When reductants were added, the Fe<sub>3</sub>O<sub>4</sub> shell of the matte droplets (Fig. 8(e)) in the original slag can be eliminated by reduction. Compared with the pure pyrite powder, the (FeS<sub>2</sub>+C) composite pellet possesses a stronger reduction ability, which contributes to the release of many wrapped copper matte droplets and results in the easy collision of matte droplets for enhanced growth (Fig. 8(f) and (g)).

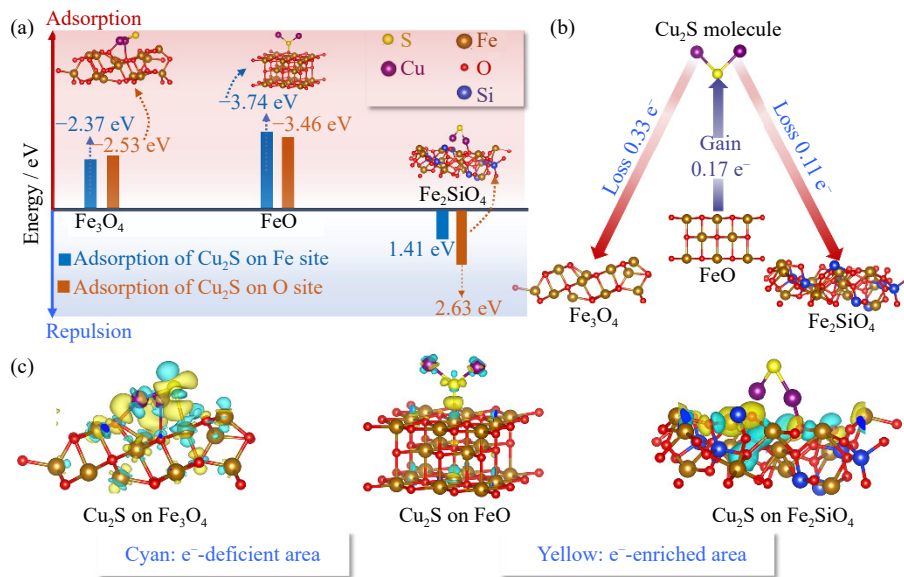
Fe<sub>3</sub>O<sub>4</sub> reduction promotes the exposure of the wrapped copper matte droplets, and the subsequent size growth can



**Fig. 8.** SEM images for the copper slag in the lower layer after reduction by various reductants: (a) original copper slag; (b) reduction by pyrite powder; (c) reduction by (FeS<sub>2</sub>+C) pellet; (d) statistical analysis results for the extent of copper matte encapsulation by Fe<sub>3</sub>O<sub>4</sub> shell; (e–g) illustration for breaking the Fe<sub>3</sub>O<sub>4</sub>-wrapped copper microstructure: (e) original copper slag, (f) reduced by FeS<sub>2</sub> powder, and (g) reduced by (FeS<sub>2</sub>+C) pellets.

also be explained by the DFT results. As shown in Fig. 9(a), the adsorption energies of Cu<sub>2</sub>S molecules on Fe<sub>3</sub>O<sub>4</sub> and FeO presented minor values, meaning the adsorption can occur spontaneously. Cu<sub>2</sub>S–Fe<sub>2</sub>SiO<sub>4</sub> exhibited a repulsion behavior, as shown by the positive adsorption energy (Fig. 9(a)). Therefore, the precipitated Fe<sub>3</sub>O<sub>4</sub> particles can preferentially adhere to the copper matte droplets, finally resulting in the Fe<sub>3</sub>O<sub>4</sub>-wrapped copper structure with the continuous growth of the Fe<sub>3</sub>O<sub>4</sub> particle size. During the reduction, Fe<sub>3</sub>O<sub>4</sub> was converted to FeO, which can combine with SiO<sub>2</sub> to generate liquid Fe<sub>2</sub>SiO<sub>4</sub>, freeing the copper matte droplets from being wrapped. Moreover, the repulsion behavior between Cu<sub>2</sub>S

and Fe<sub>2</sub>SiO<sub>4</sub> means that the Fe<sub>2</sub>SiO<sub>4</sub> that solidified during the cooling will not wrap the copper matte droplets again, similar to the Fe<sub>3</sub>O<sub>4</sub> in the molten slag, therefore enabling the free-standing states of copper matte droplets in cold slag. The preferential adsorption of Cu<sub>2</sub>S on the Fe<sub>3</sub>O<sub>4</sub> was also manifested by the Bader electrons distribution analysis (Fig. 9(b)), showing that the Cu<sub>2</sub>S–Fe<sub>3</sub>O<sub>4</sub> electron transfer value (0.33) was higher than that of Cu<sub>2</sub>S–FeO (0.17) and Cu<sub>2</sub>S–Fe<sub>2</sub>SiO<sub>4</sub> (0.11). Such stronger interaction between Cu<sub>2</sub>S and Fe<sub>3</sub>O<sub>4</sub> was also implied by the differential charge density (Fig. 9(c)) as shown by the strongest electron interactions between Cu<sub>2</sub>S and Fe<sub>3</sub>O<sub>4</sub> among the investigated three cases.



**Fig. 9.** DFT calculations for the interactions of Cu<sub>2</sub>S molecules on Fe<sub>3</sub>O<sub>4</sub>, FeO, and Fe<sub>2</sub>SiO<sub>4</sub>: (a) adsorption energies of Cu<sub>2</sub>S molecule on different structures and their illustrations; (b) Bader electron distributions; (c) differential charge density. Cyan and yellow represent the loss of 5 charges per cubic nanometer and the gain of 5 charges per cubic nanometer, respectively.

The formation of the Fe<sub>3</sub>O<sub>4</sub>-wrapped copper structure is due to the preferential adsorption of Cu<sub>2</sub>S on the precipitated Fe<sub>3</sub>O<sub>4</sub> particles. Replacing the powdery pyrite or anthracite with the (FeS<sub>2</sub>+C) pellets as the reductants can greatly enhance the reduction efficiency of the Fe<sub>3</sub>O<sub>4</sub> particles in the molten slag, resulting in a fracture in the Fe<sub>3</sub>O<sub>4</sub>-wrapped copper microstructure and the full exposure of the copper cores. This phenomenon contributed to the coalescence-induced size growth and promoted the settling of the copper matte droplets. The adsorption of the released copper matte droplets by the precipitated Fe<sub>2</sub>SiO<sub>4</sub> can hardly take place during cooling due to the Cu<sub>2</sub>S–Fe<sub>2</sub>SiO<sub>4</sub> repulsion behavior. As a consequence, the copper–slag separation was greatly enhanced.

### 3.3. Enhanced copper matte settling correlating with the change in the physicochemical properties of slag

In addition to increased size, the enhanced settling of the copper matte droplets was also attributed to the optimized physicochemical properties of the slag, namely, decreased viscosity and lowered melting point. As mentioned previously, Eq. (3) was applied to describe the viscous behavior of liquid melts containing solid phases. Fig. 10(a) shows that at

fixed temperatures, the viscosity ( $\mu$ ) of the slag was greatly affected by the content of the solid phase. As shown in Fig. 10(b), the phase diagram indicated a small liquid phase next to the crystalline region. The conversion of Fe<sub>3</sub>O<sub>4</sub> to FeO dragged the slag composition from the spinel phase region for the original slag (slag liquid + spinel, marked as point 1) to the fully melted area cases (slag (liquid)). When the content of Fe<sub>3</sub>O<sub>4</sub> was decreased to at least 8.9wt% (marked as point 2), the slag composition began to shift from the spinel region to the slag liquid region. The composition for the (FeS<sub>2</sub>+C) pellet-treated slag was closest to the center of the slag liquid region (marked as point 3 in Fig. 10), leading to the low viscosity of the molten slag.

The most efficient conversion of Fe<sub>3</sub>O<sub>4</sub> to FeO for the (FeS<sub>2</sub>+C) pellet among the three tested cases was also revealed by the XPS results. Fig. 11(a) shows that for the reductant of C powder, the ratio of Fe<sup>3+</sup>/Fe<sup>2+</sup> in the posttreated slag was 0.63, indicating that 39% iron exists as Fe<sup>3+</sup> in the sample. For the reductant of FeS<sub>2</sub> powder, the ratio of Fe<sup>3+</sup>/Fe<sup>2+</sup> in the posttreated slag was 0.72; that is, 42% iron exists as Fe<sup>3+</sup> in the sample. For the (FeS<sub>2</sub>+C) pellet, the ratio of Fe<sup>3+</sup>/Fe<sup>2+</sup> in the posttreated slag was only 0.27, showing that 21% iron exists as Fe<sup>3+</sup> in the sample. These results im-

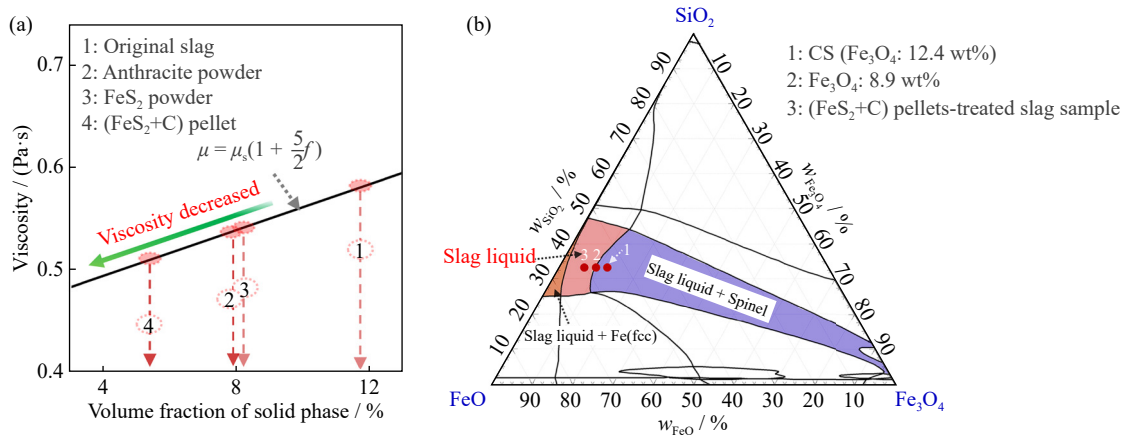


Fig. 10. (a) Liquid viscosity is described by a function of the solid-phase volume fraction; (b) slag composition evolution in the 1250°C-isothermal FeO–SiO<sub>2</sub>–Fe<sub>3</sub>O<sub>4</sub> phase diagram.

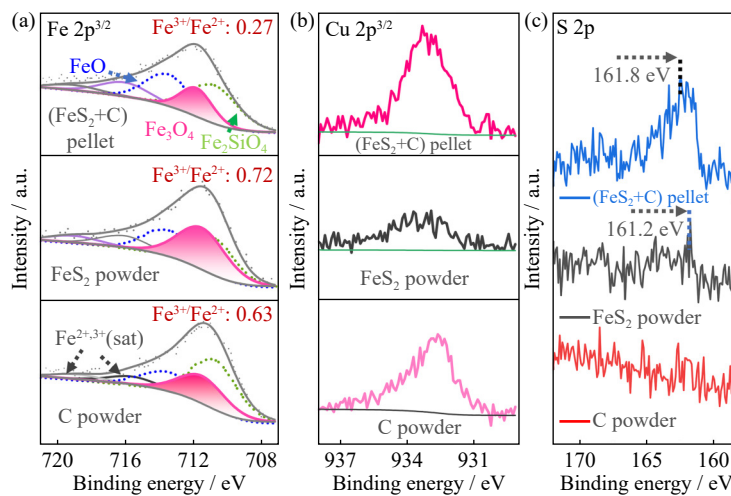


Fig. 11. XPS analysis for various posttreated slags in the lower layer: (a) Fe 2p<sup>3/2</sup> spectrum; (b) Cu 2p<sup>3/2</sup> spectrum; (c) S 2p spectrum.

ply that the (FeS<sub>2</sub>+C) pellet contributes to a deep reduction of trivalent iron in the slag, and an amount of free FeO reacts with SiO<sub>2</sub> at high temperatures to form the low-melting-point substance fayalite (Fe<sub>2</sub>SiO<sub>4</sub>). Efficient Fe<sub>3</sub>O<sub>4</sub> reduction promoting the exposure of wrapped copper matte droplets was also manifested by the strongest spectra of Cu 2p<sup>3/2</sup> and S 2p in the (FeS<sub>2</sub>+C) pellet case (Fig. 11(b) and (c)).

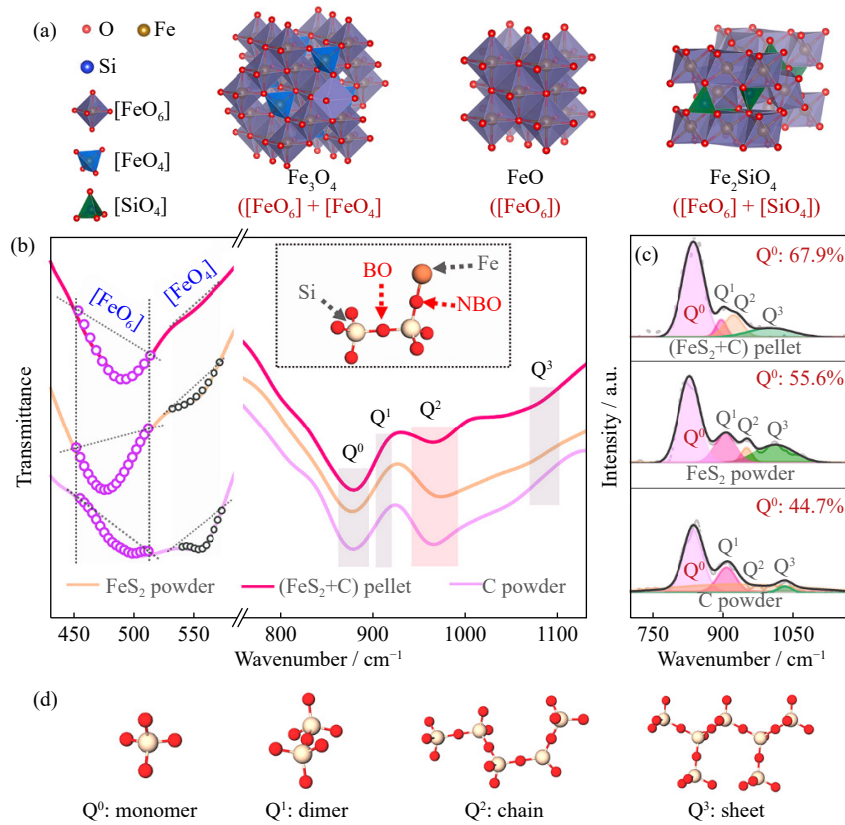
The most efficient conversion of Fe<sub>3</sub>O<sub>4</sub> to FeO by the (FeS<sub>2</sub>+C) pellet was also revealed by Raman and FTIR characterizations. The Si–O structures were depolymerized to facilitate the decrease in slag viscosity [37]. Fig. 12(a) shows that for the Fe–O coordinated structures, the Fe<sub>3</sub>O<sub>4</sub> contains the tetrahedral coordinated structure ([FeO<sub>4</sub>]) and octahedral coordinated structure ([FeO<sub>6</sub>]); however, the FeO and Fe<sub>2</sub>SiO<sub>4</sub> only present the octahedral [FeO<sub>6</sub>] coordinated structure. The [FeO<sub>6</sub>] and [FeO<sub>4</sub>] coordinated structures present characteristic peaks at 450–520 and 535–575 cm<sup>-1</sup>, respectively, in the FTIR spectra [52–54] and show the weakest [FeO<sub>4</sub>] peak for the (FeS<sub>2</sub>+C) pellet case (Fig. 12(b)). This finding again proves the most efficient conversion of Fe<sub>3</sub>O<sub>4</sub> to FeO by the (FeS<sub>2</sub>+C) pellets among the three tested cases. The generated FeO can provide free oxygen to break the polymerized silicate network, thus decreasing the

slag viscosity [55]. This anticipation was verified by the FTIR (Fig. 12(b)) and Raman (Fig. 12(c)) results. As shown in Fig. 12(b), the FTIR signal in 850–1100 cm<sup>-1</sup> is attributed to the four Si–O structures of Q<sup>0</sup> (monomer), Q<sup>1</sup> (dimer), Q<sup>2</sup> (chain), and Q<sup>3</sup> (sheet) [38,54] as illustrated in Fig. 12(d). The intensity of Q<sup>2</sup> and Q<sup>3</sup> shows the weakest for the (FeS<sub>2</sub>+C) pellet sample, indicating the lowest content of bridged oxygen (denoted as BO in the inset of Fig. 12(b)) that contributes to the decrease in slag viscosity [56]. Such results were again validated by the Raman spectra, as shown by the highest relative content of Q<sup>0</sup> (67.9%), namely, the highest content of nonbridged oxygen (denoted as NBO in the inset of Fig. 12(b)).

Therefore, the (FeS<sub>2</sub>+C) pellet enables the efficient reduction of Fe<sub>3</sub>O<sub>4</sub> to FeO, decreasing the volume fraction of solid particles in the molten slag and contributing to viscosity reduction. In addition, the high-efficiency reduction of Fe<sub>3</sub>O<sub>4</sub> can also provide additional basic FeO species, which can act as donors of free oxygen ions and strongly combine with the acid SiO<sub>2</sub> for the structure depolymerization of the silicates, realizing a decrease in the slag viscosity.

The formation of the Fe<sub>3</sub>O<sub>4</sub>-wrapped copper structure is due to the preferential adsorption of Cu<sub>2</sub>S on the precipitated





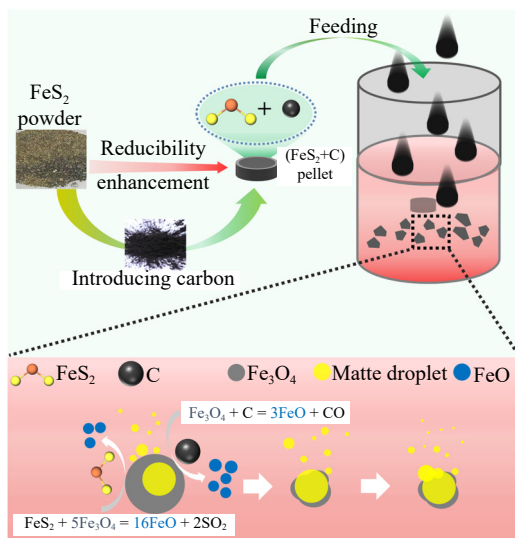
**Fig. 12.** (a) Illustration for the crystalline structures of Fe<sub>3</sub>O<sub>4</sub>, FeO, and Fe<sub>2</sub>SiO<sub>4</sub>; (b) FTIR spectra of three posttreated slags. Inset: illustration of the bridged oxygen (BO) and nonbridged oxygen (NBO); (c) Raman spectrum of three posttreated slags; (d) illustration for Si–O polymerized structures.

Fe<sub>3</sub>O<sub>4</sub> particles. Replacing the powdery pyrite or anthracite with the (FeS<sub>2</sub>+C) pellets as the reductants (Fig. 13) can greatly enhance the reduction efficiency of the Fe<sub>3</sub>O<sub>4</sub> particles in the molten slag, resulting in a fracture in the Fe<sub>3</sub>O<sub>4</sub>-wrapped copper microstructure and the full exposure of the matte cores and contributing to the coalescence-induced size growth and promoted settling of the matte droplets. In addition, Fe<sub>3</sub>O<sub>4</sub> reduction can contribute to de-

creased solid contents in molten slag, and the Fe<sub>3</sub>O<sub>4</sub>-reduction-generated FeO can promote the depolymerization of the silicates, conjointly lowering the viscosity of the molten slag. As a consequence, the copper–slag separation is greatly enhanced.

### 4. Conclusion

The formation of the Fe<sub>3</sub>O<sub>4</sub>-wrapped copper structure in Fe<sub>3</sub>O<sub>4</sub>-saturated slag is discussed, and Fe<sub>3</sub>O<sub>4</sub> is reduced using various reductants to promote the release of the wrapped copper matte droplets. The copper matte can spontaneously adhere to the precipitated Fe<sub>3</sub>O<sub>4</sub> particles, finally resulting in the Fe<sub>3</sub>O<sub>4</sub>-wrapped copper structure with the continuous growth of the Fe<sub>3</sub>O<sub>4</sub> particles. Replacing the commercial powdery pyrite or anthracite with the (FeS<sub>2</sub>+C) pellets as the reductants can greatly enhance the reduction efficiency of the Fe<sub>3</sub>O<sub>4</sub> particles in the molten slag, resulting in a fracture in the Fe<sub>3</sub>O<sub>4</sub>-wrapped copper microstructure and the full exposure of the copper matte cores. This phenomenon is one of the important reasons for the increase in the size of copper matte droplets in the lower layer from 25 μm to a size observable by the naked eye. Correspondingly, the reduction efficiency of Fe<sub>3</sub>O<sub>4</sub> in the lower layer of the slag increases significantly to 56.1wt% in the optimized case, with the copper content in the lower layer of the slag increasing remarkably from 1.2wt% to 4.5wt%. Hopefully, anthracite can be replaced by other low-quality coals, such as bituminous coal, which will



**Fig. 13.** Illustration for the enhanced collision and settling of copper matte particles by (FeS<sub>2</sub>+C) pellets in magnetite-saturated copper slags.

be investigated in future work. The results provide new insights into the enhanced *in-situ* enrichment of copper from pyrometallurgical molten slag.

## Acknowledgements

This work was financially supported by the National Natural Science Foundation of China (No. 52274349), the National Key Basic Research and Development Program of China (No. 2022YFC3900801), the Fujian Province University-Industry Cooperation Research Program, China (No. 2023H6007), and the Fujian Province Natural Science Foundation, China (No. 2023J05024).

We thank Xin Wang at the Analysis and Testing Center of the Institute of Hydrobiology, Chinese Academy of Sciences, for experimental support.

## Conflict of Interest

The authors declare no competing financial interest.

## References

- [1] S.Q. Nie, Y. Xin, Q.Y. Wang, *et al.*, Three-dimensional structural Cu<sub>6</sub>Sn<sub>5</sub>/carbon nanotubes alloy thin-film electrodes fabricated by *in situ* electrodeposition from the leaching solution of waste-printed circuit boards, *Int. J. Miner. Metall. Mater.*, 30(2023), No. 6, p. 1171.
- [2] X. Li, B.Z. Ma, C.Y. Wang, D. Hu, Y.W. Lü, and Y.Q. Chen, Recycling and recovery of spent copper–indium–gallium–diselenide (CIGS) solar cells: A review, *Int. J. Miner. Metall. Mater.*, 30(2023), No. 6, p. 989.
- [3] D. Wang, Q. Ma, K.H. Tian, C.Q. Duan, Z.Y. Wang, and Y.G. Liu, Ultrafine nano-scale Cu<sub>2</sub>Sb alloy confined in three-dimensional porous carbon as an anode for sodium-ion and potassium-ion batteries, *Int. J. Miner. Metall. Mater.*, 28(2021), No. 10, p. 1666.
- [4] M. Hao, L.B. Tang, P. Wang, *et al.*, Mapping China's copper cycle from 1950–2015: Role of international trade and secondary resources, *Resour. Conserv. Recycl.*, 188(2023), art. No. 106700.
- [5] S. Liu, W. Liu, Q.Y. Tan, J.H. Li, W.Q. Qin, and C.R. Yang, The impact of China's import ban on global copper scrap flow network and the domestic copper sustainability, *Resour. Conserv. Recycl.*, 169(2021), art. No. 105525.
- [6] R. Sridhar, J.M. Toguri, and S. Simeonov, Copper losses and thermodynamic considerations in copper smelting, *Metall. Mater. Trans. B*, 28(1997), No. 2, p. 191.
- [7] Q.M. Wang, S.S. Wang, M. Tian, D.X. Tang, Q.H. Tian, and X.Y. Guo, Relationship between copper content of slag and matte in the SKS copper smelting process, *Int. J. Miner. Metall. Mater.*, 26(2019), No. 3, p. 301.
- [8] Z. Zivkovic, P. Djordjevic, and N. Mitevska, Contribution to the examination of the mechanisms of copper loss with the slag in the process of sulfide concentrates smelting, *Min. Metall. Explor.*, 37(2020), No. 1, p. 267.
- [9] G.R. Qu, Y.G. Wei, B. Li, H. Wang, Y.D. Yang, and A. McLean, Distribution of copper and iron components with hydrogen reduction of copper slag, *J. Alloys Compd.*, 824(2020), art. No. 153910.
- [10] H.P. Zhang, B. Li, A. McLean, Y.G. Wei, H. Wang, and Z.L. Ye, Investigation of reducing copper slag using waste motor oil to recover matte, *Metall. Mater. Trans. B*, 54(2023), No. 1, p. 178.
- [11] S.W. Zhou, Y.G. Wei, S.Y. Zhang, *et al.*, Reduction of copper smelting slag using waste cooking oil, *J. Cleaner. Prod.*, 236(2019), art. No. 117668.
- [12] S.W. Zhou, Y.G. Wei, Y. Shi, B. Li, and H. Wang, Characterization and recovery of copper from converter copper slag via smelting separation, *Metall. Mater. Trans. B*, 49(2018), No. 5, p. 2458.
- [13] Z.L. Ye, G.P. Dai, B. Zhang, *et al.*, Apparent viscosity evolution of copper converter slag during a reduction process, *Min. Metall. Explor.*, 39(2022), No. 6, p. 2529.
- [14] F. Yuan, Z. Zhao, Y.L. Zhang, and T. Wu, Effect of Al<sub>2</sub>O<sub>3</sub> content on the viscosity and structure of CaO–SiO<sub>2</sub>–Cr<sub>2</sub>O<sub>3</sub>–Al<sub>2</sub>O<sub>3</sub> slags, *Int. J. Miner. Metall. Mater.*, 29(2022), No. 8, p. 1522.
- [15] E. De Wilde, I. Bellemans, M. Campforts, *et al.*, Study of the effect of spinel composition on metallic copper losses in slags, *J. Sustainable Metall.*, 3(2017), No. 2, p. 416.
- [16] J. Isaksson, A. Andersson, T. Vikström, A. Lennartsson, and C. Samuelsson, Improved settling mechanisms of an industrial copper smelting slag by CaO modification, *J. Sustainable Metall.*, 9(2023), No. 3, p. 1378.
- [17] H.Y. Wang, R. Zhu, K. Dong, S.Q. Zhang, Y. Wang, and X.Y. Lan, Effect of injection of different gases on removal of arsenic in form of dust from molten copper smelting slag prior to recovery process, *Trans. Nonferrous Met. Soc. China*, 33(2023), No. 4, p. 1258.
- [18] X. Gao, Z. Chen, J.J. Shi, P. Taskinen, and A. Jokilaakso, Effect of cooling rate and slag modification on the copper matte in smelting slag, *Min. Metall. Explor.*, 37(2020), No. 5, p. 1593.
- [19] A. Sarrafi, B. Rahmati, H.R. Hassani, and H.H.A. Shirazi, Recovery of copper from reverberatory furnace slag by flotation, *Miner. Eng.*, 17(2004), No. 3, p. 457.
- [20] B. Inge, D.W. Evelien, M. Nele, and V. Kim, Metal losses in pyrometallurgical operations: A review, *Adv. Colloid Interface Sci.*, 255(2018), p. 47.
- [21] Z.Q. Guo, D.Q. Zhu, J. Pan, F. Zhang, and C.C. Yang, Industrial tests to modify molten copper slag for improvement of copper recovery, *JOM*, 70(2018), No. 4, p. 533.
- [22] H.P. Zhang, B. Li, Y.G. Wei, and H. Wang, The settling behavior of matte particles in copper slag and the new technology of copper slag cleaning, *J. Mater. Res. Technol.*, 15(2021), p. 6216.
- [23] H.H. Zhou, G.J. Liu, L.Q. Zhang, and C.C. Zhou, Mineralogical and morphological factors affecting the separation of copper and arsenic in flash copper smelting slag flotation beneficiation process, *J. Hazard. Mater.*, 401(2021), art. No. 123293.
- [24] X.S. Guo, Z.Y. Li, J.C. Han, D. Yang, and T.C. Sun, Petroleum coke as reductant in co-reduction of low-grade laterite ore and red mud to prepare ferronickel: Reductant and reduction effects, *Int. J. Miner. Metall. Mater.*, 29(2022), No. 3, p. 455.
- [25] H.P. Zhang, B. Li, Y.G. Wei, H. Wang, Y.D. Yang, and A. McLean, Reduction of magnetite from copper smelting slag in the presence of a graphite rod, *Metall. Mater. Trans. B*, 51(2020), No. 6, p. 2663.
- [26] H.Q. Zhang, G.H. Chen, X. Cai, *et al.*, The leaching behavior of copper and iron recovery from reduction roasting pyrite cinder, *J. Hazard. Mater.*, 420(2021), art. No. 126561.
- [27] B.J. Zhang, T.A. Zhang, Z.H. Dou, and D.L. Zhang, Effect of vortex stirring on the dilution of copper slag, *J. Wuhan Univ. Technol. Mater Sci Ed*, 37(2022), No. 4, p. 699.
- [28] N. Dosmukhamedov, M. Egizekov, E. Zholdasbay, and V. Kaplan, Metal recovery from converter slags using a sulfiding agent, *JOM*, 70(2018), No. 10, p. 2400.
- [29] S.W. Zhou, Y.G. Wei, B. Li, and H. Wang, Effect of iron phase evolution on copper separation from slag via coal-based reduction, *Metall. Mater. Trans. B*, 49(2018), No. 6, p. 3086.
- [30] B.J. Zhang, T.A. Zhang, L.P. Niu, N.S. Liu, Z.H. Dou, and Z.Q.

- Li, Moderate dilution of copper slag by natural gas, *JOM*, 70(2018), No. 1, p. 47.
- [31] J. Zhang, Y.H. Qi, D.L. Yan, and H.C. Xu, A new technology for copper slag reduction to get molten iron and copper matte, *J. Iron Steel Res. Int.*, 22(2015), No. 5, p. 396.
- [32] I.P. Plotnikov, A.A. Komkov, and S.V. Bystrov, Behavior of copper and sulfur during high-temperature sulfurization of copper-smelting slags with elemental sulfur, *Metallurgist*, 67(2023), No. 3, p. 476.
- [33] F. Yin, P. Xing, Q. Li, C.Y. Wang, and Z. Wang, Magnetic separation-sulphuric acid leaching of Cu–Co–Fe matte obtained from copper converter slag for recovering Cu and Co, *Hydrometallurgy*, 149(2014), p. 189.
- [34] S. Hughes, Applying ausmelt technology to recover Cu, Ni, and Co from slags, *JOM*, 52(2000), No. 8, p. 30.
- [35] J. Isaksson, A. Andersson, A. Lennartsson, and C. Samuelsson, Interactions of crucible materials with an FeO<sub>x</sub>–SiO<sub>2</sub>–Al<sub>2</sub>O<sub>3</sub> melt and their influence on viscosity measurements, *Metall. Mater. Trans. B*, 54(2023), No. 6, p. 3526.
- [36] H. Saigo, D.B. Kc, and N. Saito, Einstein–Roscoe regression for the slag viscosity prediction problem in steelmaking, *Sci. Rep.*, 12(2022), No. 1, art. No. 6541.
- [37] T.S. Kim and J.H. Park, Structure–viscosity relationship of low-silica calcium aluminosilicate melts, *ISIJ Int.*, 54(2014), No. 9, p. 2031.
- [38] Y. Shi, Y.G. Wei, S.W. Zhou, B. Li, Y.D. Yang, and H. Wang, Effect of B<sub>2</sub>O<sub>3</sub> content on the viscosity of copper slag, *J. Alloys Compd.*, 822(2020), art. No. 153478.
- [39] A. Rusen, A. Geveci, Y. Ali Topkaya, and B. Derin, Effects of some additives on copper losses to matte smelting slag, *JOM*, 68(2016), No. 9, p. 2323.
- [40] P. Hohenberg and W. Kohn, Inhomogeneous electron gas, *Phys. Rev.*, 136(1964), No. 3B, p. 864.
- [41] W. Kohn and L.J. Sham, Self-consistent equations including exchange and correlation effects, *Phys. Rev.*, 140(1965), No. 4A, p. A1133.
- [42] P.E. Blöchl, Projector augmented-wave method, *Phys. Rev. B: Condens. Matter*, 50(1994), No. 24, p. 17953.
- [43] S.P. Zhong, H.L. Zhu, L. Yang, X.P. Chi, W. Tan, and W. Weng, Activating bulk nickel foam for the electrochemical oxidation of ethanol by anchoring MnO<sub>2</sub>@Au nanorods, *J. Mater. Chem. A*, 11(2023), No. 15, p. 8101.
- [44] W. Weng, J.X. Xiao, Y.J. Shen, X.X. Liang, T. Lv, and W. Xiao, Molten salt electrochemical modulation of iron–carbon–nitrogen for lithium–sulfur batteries, *Angew. Chem. Int. Ed.*, 60(2021), No. 47, p. 24905.
- [45] J.K. Nørskov, T. Bligaard, A. Logadottir, et al., Trends in the exchange current for hydrogen evolution, *J. Electrochem. Soc.*, 152(2005), art. No. J23.
- [46] J.K. Nørskov, J. Rossmeisl, A. Logadottir, et al., Origin of the overpotential for oxygen reduction at a fuel-cell cathode, *J. Phys. Chem. B*, 108(2004), No. 46, p. 17886.
- [47] B. Zhang, J. Liu, J.S. Wang, et al., Interface engineering: The Ni(OH)<sub>2</sub>/MoS<sub>2</sub> heterostructure for highly efficient alkaline hydrogen evolution, *Nano Energy*, 37(2017), p. 74.
- [48] Y. Ke, N. Peng, K. Xue, et al., Sulfidation behavior and mechanism of zinc silicate roasted with pyrite, *Appl. Surf. Sci.*, 435(2018), p. 1011.
- [49] K. Wang, Y. Liu, J. Hao, Z.H. Dou, G.Z. Lv, and T.A. Zhang, A novel slag cleaning method to recover copper from molten copper converter slag, *Trans. Nonferrous Met. Soc. China*, 33(2023), No. 8, p. 2511.
- [50] H.M. Ferreira, E.B. Lopes, J.F. Malta, et al., Preparation and densification of bulk pyrite, FeS<sub>2</sub>, *J. Phys. Chem. Solids*, 159(2021), art. No. 110296.
- [51] M. Kuosa, B. Ekberg, L. Tanttu, T. Jauhiainen, and A. Häkkinen, Performance comparison of anthracite filter media of different origin in the removal of organic traces from copper electrolyte, *Int. J. Miner. Process.*, 163(2017), p. 24.
- [52] A. Rajan, M. Sharma, and N.K. Sahu, Assessing magnetic and inductive thermal properties of various surfactants functionalised Fe<sub>3</sub>O<sub>4</sub> nanoparticles for hyperthermia, *Sci. Rep.*, 10(2020), No. 1, art. No. 15045.
- [53] R. Jain and S. Gulati, Influence of Fe<sup>2+</sup> substitution on FTIR and Raman spectra of Mn ferrite nanoparticles, *Vib. Spectrosc.*, 126(2023), art. No. 103540.
- [54] R.L. Zheng, J.F. Lü, W.F. Song, et al., Metallurgical properties of CaO–SiO<sub>2</sub>–Al<sub>2</sub>O<sub>3</sub>–4.6wt%MgO–Fe<sub>2</sub>O<sub>3</sub> slag system pertaining to spent automotive catalyst smelting, *Int. J. Miner. Metall. Mater.*, 30(2023), No. 5, p. 886.
- [55] S.F. Ma, K.J. Li, J.L. Zhang, et al., The effects of CaO and FeO on the structure and properties of aluminosilicate system: A molecular dynamics study, *J. Mol. Liq.*, 325(2021), art. No. 115106.
- [56] T. Talapaneni, N. Yedla, S. Pal, and S. Sarkar, Experimental and theoretical studies on the viscosity–structure correlation for high alumina–silicate melts, *Metall. Mater. Trans. B*, 48(2017), No. 3, p. 1450.